Conformational disorder in quercetin dihydrate revealed from ultrahigh-resolution synchrotron diffraction

Yvon Bibila Mayaya Bisseyou, Jonathan Wright, Christian Jelsch

STRUCTURAL SCIENCE
CRYSTAL ENGINEERING
MATERIALS

ISSN: 2052-5206
journals.iucr.org/b

Conformational disorder in quercetin dihydrate revealed from ultrahigh-resolution synchrotron diffraction

Yvon Bibila Mayaya Bisseyou, Jonathan Wright and Christian Jelsch

Acta Cryst. (2024). B**80**, 766–781

Acta Cryst B STRUCTURAL SCIENCE CRYSTAL ENGINEERING MATERIALS

ISSN 2052-5206

Conformational disorder in quercetin dihydrate revealed from ultrahigh-resolution synchrotron diffraction

Yvon Bibila Mayaya Bisseyou,[a] Jonathan Wright[b] and Christian Jelsch[c]*

[a]Laboratoire des Sciences de la Matière, de l'Environnement et de l'Energie, Solaire, UFR SSMT, Université Félix Houphouët-Boigny, BP 582 Abidjan 22, Cote d'Ivoire, [b]European Synchrotron Radiation Facility, 71 Avenue des Martyrs, 38000 Grenoble, France, and [c]CRM2, UMR CNRS 7036, Université de Lorraine, 54500 Nancy, France. *Correspondence e-mail: christian.jelsch@univ-lorraine.fr

Received 2 August 2024
Accepted 12 October 2024

Edited by P. Macchi, Politecnico di Milano, Italy

Keywords: polyphenol; charge density; electrostatic complementarity; conformational disorder; Hirshfeld surface analysis.

CCDC reference: 2327707

Supporting information: this article has supporting information at journals.iucr.org/b

Quercetin, a bioflavonoid abundant in plants, boasts antioxidant properties and plays a crucial role in various biological systems. The diffraction data of a quercetin dihydrate crystal have been measured at 20 (2) K to ultrahigh resolution (0.30 Å) using a synchrotron X-ray source. After meticulous multipolar refinement of the charge density, Fourier residual electron density peaks were identified, particularly at the position of hydrogen atom H15 of the catechol ring. This observation revealed a subtle disorder in the molecule, prompting the modelling of the catechol ring in two positions with occupancy percentages of 98.4% and 1.6% in the *anti* and *syn* conformations, respectively. Intermolecular interactions are analysed using Hirshfeld fingerprint plots and enrichment ratios. With the presence of numerous O—H···O hydrogen bonds, the packing shows good electrostatic complementarity between the quercetin molecule and its surroundings. The parallel displaced stacking interaction between two *anti*-quercetin molecules related by a translation along the *a* axis is, however, not attractive for its electrostatic contribution. The *syn* conformation shows more attractive quercetin dimers than the *anti* one. On the other hand, electrostatic interactions between quercetin and the two water molecules are stronger in the *anti* conformation. The electrostatic interactions of quercetin with human inositol polyphosphate multikinase were analysed in the structure of the complex found in the Protein Data Bank and compared with those the take place in the quercetin crystal packing.

1. Introduction

Quercetin [2-(3,4-dihydroxy-phenyl)-3,5,7-trihydroxy-4*H*-chromen-4-one ($C_{15}H_{10}O_7$)] (Fig. 1) is the most extensively studied flavonoid due to its wide range of health benefits (Kumar *et al.* 2017). It is produced from natural raw material and is found in abundance in vegetables, herbs and fruit. Quercetin exhibits several medicinal properties including antioxidant (Lamson & Brignall, 2000), anticancer (Zamin *et al.*, 2009; Deng *et al.*, 2013), anti-hypertensive (Duarte *et al.*, 2001), anti-inflammatory (Oršolić *et al.*, 2004), anti-microbial (Gatto *et al.*, 2002; Cushnie & Lamb, 2005), anti-coagulative (Bucki *et al.*, 2003) and cardiovascular activities. It is also used in neurodegenerative diseases as a neuroprotective agent. Indeed, Islam *et al.* (2013) have reported its acetylcholinesterase inhibitory effect and Magalingam *et al.* (2014) have highlighted the neuroprotective role of isoquercetin (glycoside form of quercetin) against 6-OHDA-induced neurotoxicity in PC12 cells. Recently, Shi *et al.* (2019) have proved that quercetin protects against diabetes and its complications, and is a promising molecule for the treatment of these diseases.

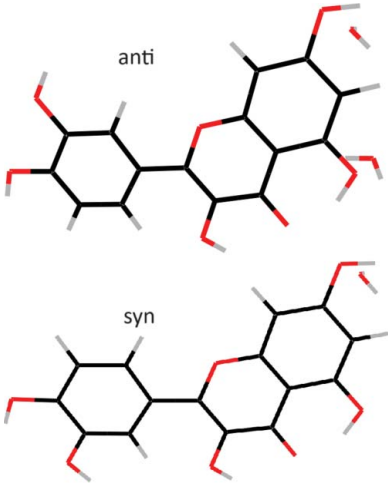

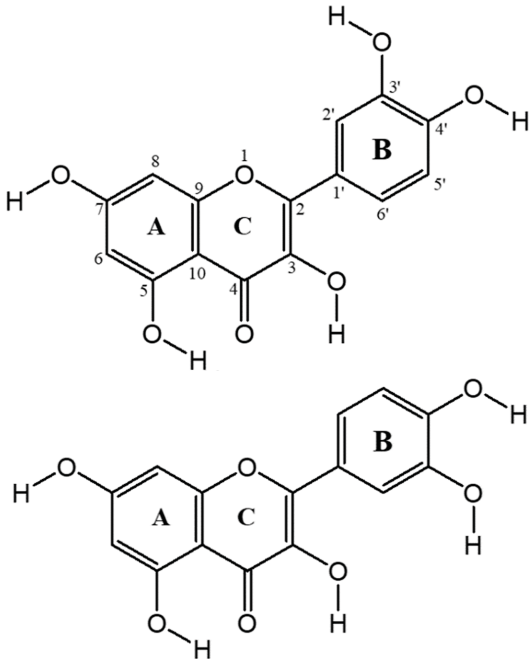

Figure 1
Molecular scheme of quercetin: (top) the major *anti* component, (bottom) the minor *syn* component.

Gu *et al.* (2019) also showed that quercetin and 16 related flavonoids are inhibitors of two human kinases: human inositol polyphosphate multikinase (hIPMK) and human hexakisphosphate kinase. The latter protein was recently revealed and classified as a new target for anticancer treatments (Minini *et al.*, 2020).

Because of the multifariousness of its functions and taking into account the pharmaceutical stake, the quercetin molecule gained interest and has been the subject of many studies. One of the main purposes of these studies is the accurate analysis of its electronic and molecular structure. This analysis is crucial for understanding redox properties of quercetin.

Three solid crystalline structures of quercetin are known: anhydrate (Olejniczak & Potrzebowski, 2004; Filip *et al.*, 2013), monohydrate (Domagała *et al.*, 2011) and dihydrate (Olejniczak & Potrzebowski, 2004; Rossi *et al.*, 1986; Jin *et al.*, 1990). In these molecular structures, some discrepancies have been observed in the geometry at the level of the catechol ring conformation, which exhibits free rotations around the C—C bond to the pyrone ring system. The catechol skeleton adopts a *syn* conformation in the anhydrate and monohydrate, while it is *anti* in the dihydrate form (Fig. 1). Moreover, the solid-state conformational study of pure quercetin using ^{13}C-CP-MAS-NMR techniques, conducted by Wawer & Zielinska (1997), revealed the existence of conformers *anti*. Even though high-resolution solid-state NMR and density functional theory calculations suggested the presence of a *syn* conformer in the solid state (Olejniczak & Potrzebowski, 2004), a stronger proof, such as employing single-crystal X-ray diffraction to confirm the presence of the *syn* form, was still missing (Olejniczak & Potrzebowski, 2004).

Theoretical calculation studies on the quercetin structure using AM1 (Russo *et al.*, 2000), RHF/6-31G* (Vasilescu & Girma, 2002) and B3LYP/6-311++G** (Leopoldini *et al.*, 2004) levels reveal an easy rotation of the catechol moiety and a very small energy gap between the two stable conformations with the *syn* conformer preferred over the *anti* form. This study suggests the coexistence of both conformers of quercetin in a hydrate environment.

Conformational degree of freedom is correlated with the occurrence of polymorphism (Domagała *et al.*, 2011; Dubey & Desiraju, 2015).

Nearly 40 cocrystal structures of quercetin have been reported in the Cambridge Structural Database (CSD 2023) with diverse conformers, including some ternary solids (Dubey & Desiraju, 2015). An in-depth study on the conformational analysis of quercetin in the gas phase was carried out with a total of 48 stable conformations (24 planar and 24 non-planar) by varying the relative orientations of the five OH groups and non-deformable (*A* + *C*) and *B* rings (Brovarets & Hovorun, 2020*a*). Interconversions in the 24 pairs of conformers were also investigated (Brovarets & Hovorun, 2020*b*). As per this study, for the interconversion (9 [major, I *anti*] ↔ 10 [minor, II *syn*]) *via* the rotation around the C2—C1′ bond through the quasi-orthogonal transition state, the Gibbs free energy barriers for the forward and reverse directions were 22.2 kJ mol^{-1} and 22.0 kJ mol^{-1} (Brovarets & Hovorun, 2020*b*).

Recently, Klitou *et al.* (2019) reported the crystallization behaviour of the three crystal forms of the quercetin compound using synthonic modelling and molecular conformational analysis.

The quercetin is an amphipathic molecule, *i.e.* it consists of hydrophobic part formed by phenyl rings and more hydrophilic ones constituted of polar hydroxyl groups. Its solubility in water is very low at 60 mg l^{-1} (Edwards *et al.*, 2007) but much higher in organic solvents. Such compounds exhibit properties depending on the charge density of their hydrophobic and hydrophilic components.

Theoretical studies on the antioxidant activity of the quercetin molecule and its derivatives (Cai *et al.*, 2014; Zheng *et al.*, 2017; Thong *et al.*, 2019) have shown that this property is mainly due to their ability to scavenge free radicals, which strongly depends on the number and arrangement of hydroxyl groups in the molecule. The different possible mechanisms highlighted in the process of antioxidant activity of quercetin and its derivatives, namely, hydrogen atom transfer, single electron transfer followed by proton transfer and sequential proton loss electron transfer are all governed by the electron density distribution in the molecule concerned. It was shown that essentially the phenolic OH groups in *B* and *C* rings (Fig. 1) contribute to the antioxidative activities of quercetin as compared to the *A* ring (Zheng *et al.*, 2017).

Although quercetin has been shown to be a potent antioxidant, some *in vitro* and *in vivo* studies in mammals (Dorta *et al.*, 2005; Dorta *et al.*, 2008; De Marchi *et al.*, 2009; Ruiz *et al.*, 2015) have shown that it also has pro-oxidant properties. Indeed, the quercetin–mitochondria interactions lead to

an increase in O_2^- production and induce a decrease in ATP levels and impairment of the respiratory chain in liver tissue.

Since the biological activity of chemical compounds is governed mainly by their electronic interactions with biomolecules, the charge density analysis of quercetin is vital. Such a study provides reliable preliminary information on its site and mode of binding (Mladenovic *et al.*, 2009). In order to gain deep insight on the electron density distribution in the quercetin molecule at solid state as well as its chemical reactivity, we have collected synchrotron diffraction data at ultrahigh resolution ($\sin\theta_{max}/\lambda$ = 1.59 Å^{-1}) and ultralow temperature [20 (2) K].

However, the initial aim of our study, namely the refinement of experimental charge density of quercetin using the Hansen & Coppens (1978) multipolar atom model as well as the estimation of derived properties, was marred by the disorder phenomenon. Indeed, although the experimental multipolar refinement had converged, analysis of residual density revealed peaks which suggest a conformational disorder of the catechol ring system. The multipolar parameters of disordered atoms cannot be refined easily to yield unbiased experimental charge density. Indeed, in most cases, taking into account disordered atomic positions and refining simultaneously their charge density leads to an increase in the number of parameters. The improvement of the *R* factors is purely a cosmetic effect to the detriment of a reliable and physically realistic electronic density model. This limits the reliability of the information that can be derived from the model. One of the most successful attempts to date is the constrained multipolar refinement of the disordered *N*-phenylpyrrole molecule (Meindl *et al.*, 2009). However, approaches to solve the problem have nevertheless been developed (TAAM refinement, mixed model refinement) but outcomes remain mixed (Bąk *et al.*, 2009; Dittrich *et al.*, 2009; Holstein *et al.*, 2010; Dittrich *et al.*, 2016; Dittrich *et al.*, 2018).

In this study, the electron density of the quercetin molecule in its dihydrate form was determined from synchrotron ultrahigh-resolution diffraction data using Hansen–Coppens multipolar atom model (Hansen & Coppens, 1978). From a physically realistic description of electron density, the crystal structure revealed for the first time the coexistence in the crystalline state of the *anti* and *syn* conformers of quercetin which is manifested by long suspected conformational disorder (Leopoldini *et al.*, 2004). In addition, electrostatic energy (E_{elec}) of intermolecular interactions between quercetin and hIPMK, a target for the treatment of cancer (Gu *et al.*, 2019), was analysed using the aspherical atom model for the hIPMK–quercetin complex, constructed from the transferable atomic densities principle (Brock *et al.*, 1991; Domagała *et al.*, 2011). Noteworthy, electrostatic energy is the most robust component of total energy and exhibits the most significant contribution to interaction energy in biological systems. Its assessment in the enzyme inhibitor interactions provides insights into rational drug design and is crucial in the development process of new drugs.

2. Materials and methods

2.1. Crystallization

Quercetin dihydrate was purchased as a powder from Sigma–Aldrich and crystals were grown by slow evaporation method from a 1-propanol solution at room temperature. Appropriate yellow single crystals were selected for X-ray diffraction analysis.

2.2. Data collection and reduction

Diffraction data were collected on the ID11 beamline of ESRF synchrotron using a 0.15815 Å wavelength and a zero 2θ rotation angle for the two-dimensional detector. There was a single vertical rotation axis and the vertical beam size was varied to give different spots in the dynamic range of the detector. The beam size was ∼5 µm for strong, 50 µm for medium and 300 µm for weak reflections. A helium cryostream cooler device was used to maintain the temperature at 20 K during the experiment. The crystal-to-detector distance was 9 cm with 1 s exposure time. Data up to $\sin\theta/\lambda$ = 1.59 Å^{-1} were collected using 22 ω scans with a 1° rotation per frame. Data reduction was performed using *SMART*/*SAINT* (Bruker, 2008) software; empirical absorption correction was applied with *SADABS* (Bruker, 2008) and incidence angle corrections were performed. The reflections intensities were corrected using experimentally determined factors as a function of incident angle for incomplete absorption of high-energy X-rays on a CCD detector (Wu *et al.*, 2002). A total of 1145900 reflections were measured and merged into 44514 unique symmetry data, which corresponds to 99.6% completeness at the reciprocal resolution of 1.59 Å^{-1}. Further details of data collection and reduction are given in Table 1. From the Wilson (1942) plot, the global *B* factor for the current crystal structure is 0.92 Å^2.

2.3. Structure solution and spherical atom refinement

The crystal structure of the title compound was initially taken from the structure determined by Jin *et al.* (1990). The position of hydrogen atoms was checked by successive differential Fourier syntheses and a full-matrix least-squares refinement procedure using the *MoPro* program (Jelsch *et al.*, 2005) was performed with a spherical atom model. Crystal data and experimental parameters used for the intensity data collection are summarized in Table 1.

2.4. Multipolar refinement

The crystal structure was then further refined with the *MoPro* (Jelsch *et al.*, 2005) software using the multipolar atom model of Hansen & Coppens (1978). The non-disordered hydrogen atoms of quercetin were modelled as anisotropic by using the SHADE3 server (Madsen & Hoser, 2014). The distances d_{XH} of hydrogen atoms to X their carrier atom were restrained to standard neutron distances (Allen & Bruno, 2010) and chemically equivalent X—H bonds were restrained to have similar distances. H—C hydrogen atoms were in addition restrained to remain in the aromatic ring planes.

Table 1
Experimental details.

Crystal data	
Chemical formula	$C_{15}H_{10}O_7 \cdot 1.984H_2O$
M_r	337.97
Crystal system, space group	Triclinic, $P\overline{1}$
Temperature (K)	20 (2)
a, b, c (Å)	3.7244 (17), 13.050 (6), 14.982 (7)
α, β, γ (°)	71.986 (4), 83.860 (5), 85.624 (5)
V (Å^3)	687.8 (5)
Z	2
Radiation type, wavelength (Å)	Synchrotron, 0.15815
Crystal size (mm)	0.22 × 0.16 × 0.10
Data collection	
Diffractometer	Huber diffractometer, ID11/ESRF
Absorption correction	Empirical (using intensity measurements)
No. of measured, independent and observed [$I > 2\sigma(I)$] reflections	44510, 44510, 35265
R_{int}	0.065
$(\sin \theta/\lambda)_{max}$ (Å^{-1})	1.596
Refinement	
$R[F^2 > 2\sigma(F^2)]$, $wR(F^2)$, S	0.020, 0.041, 1.01
No. of reflections	44510
No. of parameters	815
No. of restraints	290
H-atom treatment	Only H-atom coordinates refined
$\Delta\rho_{max}$, $\Delta\rho_{min}$ (e Å^{-3})	0.35, −0.56

Computer programs: *MoPro* (Jelsch *et al.*, 2005), *ORTEP-3 for Windows* (Farrugia, 2012), *MoProViewer* (Guillot *et al.*, 2014), *OLEX2* (Dolomanov *et al.*, 2009).

Restraints of local symmetry and chemical equivalence were applied to the charge density of the atoms. For the atoms with partial occupancy, chemical equivalence and local symmetry constraints were applied.

Due to the higher thermal motion of the water molecules and to obtain a physically meaningful electron density, their charge density was fixed and constrained to that of the ELMAM2 database (Domagała *et al.*, 2012) and the H—O—H angle was restrained to 109.5° values. To ensure the electroneutrality of the water molecules, the valence populations of the O_{water} and H_{water} atoms were kept fixed to their database values. Moreover, the chemical equivalencies and local symmetry (two mirror planes on the oxygen atom) were applied as constraints on the water molecules. Due to the remaining residual density in the Fourier maps, six atoms of the catechol ring (C11, C12, C13, C14, O14 and O13) and the two water oxygen atoms were refined with anharmonic thermal parameters at order 4 (Fig. 2). The constraints and restraints used are documented in the CIF file.

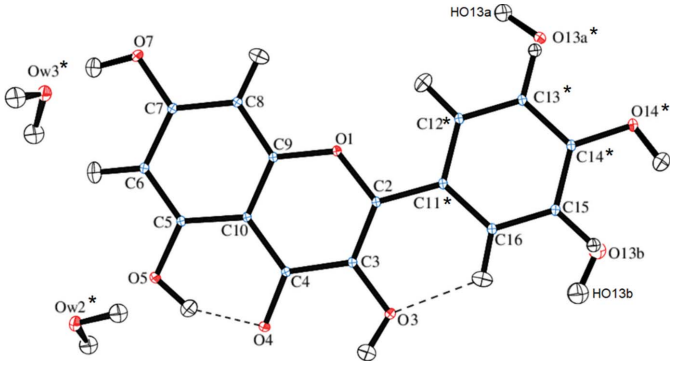

Figure 2
ORTEP plot of quercetin dihydrate with atomic numbering scheme. Displacement ellipsoids are drawn at 50% probability. The intramolecular O—H···O hydrogen bond and C—H···O interaction are plotted as dashed lines. The atoms modelled as anharmonic are marked with a * symbol.

2.5. Hirshfeld surface and contact enrichment ratios analysis

The Hirshfeld surface (Spackman & Byrom, 1997; McKinnon *et al.*, 1998; McKinnon *et al.*, 2004) specifies the space occupied by a molecule in a crystal packing. Analysis of it provides a wealth of information related to the nature and the type of intermolecular contacts experienced by the molecule in the crystal environment. Hirshfeld surface analysis and its subsequent fingerprint plots was performed using *CrystalExplorer21.5* (Spackman *et al.*, 2021) software. In addition, the contact enrichment ratio, a descriptor also derived from Hirshfeld surface analysis, was computed for each pair of chemical species with *MoProViewer* (Guillot *et al.*, 2014) software. Hirshfeld surfaces were computed using an electron density derived from the spherical neutral atom model. This descriptor is obtained from the ratio between the actual contacts with the theoretical proportions computed as if all contacts were equiprobable. The enrichment describes the over- or under-representation of contacts occurring between chemical types in the crystal packing. Mathematic details are extensively documented in the original paper by Jelsch *et al.* (2014).

2.6. Computation details of electrostatic interaction energy

Electrostatic interaction energy E_{elec} was computed with the *Charger* program (Vuković *et al.*, 2021) incorporated in the *MoProViewer* software (Guillot *et al.*, 2014). The *Charger* program is based on the analytical exact potential/multipole moments approach (Nguyen & Volkov, 2019; Nguyen *et al.*, 2020), which combines the exact potential method for short-distance interactions (Volkov, Koritsanszky *et al.*, 2004) and multipole moments approximation for non-overlapping densities for atoms at long distances (Buckingham, 1959). Coupled with the aspherical electron density model, this approach provides results with similar precision to quantum methods (Volkov, Li *et al.*, 2004). In addition, it is possible with *Charger* to assess the individual contribution of every residue to the total protein–ligand electrostatic binding energy.

The structure of the hIPMK–quercetin complex (PDB code 6m89) with resolution at 1.85 Å was retrieved from the RCSB Protein Data Bank (Gu *et al.*, 2019). This structure consists of a single monomer of hIPMK, cocrystallized with quercetin housed in its active site. The *Molprobity* (Williams *et al.*, 2018) program was used to correct some anomalies such as conformational disorder or flips of residues and to add hydrogen atoms. The hydrogen atoms of the quercetin molecule were added geometrically with the *MoPro* software.

Except the three water molecules, which contribute to the quercetin binding and hIPMK selectivity (Gu *et al.*, 2019), all other water molecules were removed. These three water molecules are involved in the interactions between hIPMK and quercetin and induce electrostatic effects, a key factor in the inhibition mode of the hIPMK enzyme by quercetin. Grädler *et al.* (2001) have highlighted the relevance of water molecules during the design of a set of novel inhibitors of tRNA–guanine transglycosylase (TGT), and Huggins & Tidor (2011) have reported the importance of water molecules in the scoring improvement of protein–ligand interactions.

Water H atoms were positioned using *PyMOL* (DeLano, 2020) and *Discovery Studio* (Biovia, 2016). All hydrogen atoms were placed according to standard neutron diffraction distances (Allen & Bruno, 2010) and no clash was observed. Geometrical parameters of these water molecules and of the resulting hydrogen-bond network are reported in Table S1. *MoPro* software was used to transfer multipolar electron-density parameters from the experimental ELMAM2 data-bank to the restored hIPMK–quercetin complex.

3. Results and discussion

3.1. Disorder and anharmonic modelling

The wR^2I factor decreased from 6.75% with spherical atom refinement to 5.15% with the multipolar atom model. There were still high residual peaks, notably around some atoms in the catechol ring area and the water molecules. Up to eight atoms were modelled as anharmonic at order 4 (C11, C12, C13, C14, O13, O14, O*W*2, O*W*3) and the wR^2I factor decreased further to 4.60%.

There was a remaining positive peak near atom H15 and negative peak near atom O13 (Fig. 3), which could be explained by a rotational disorder of the catechol ring. Moreover, the water oxygen atom O*W*2 showed residual negative density suggesting a partial occupancy. The wR^2I factor resulting from disorder modelling was then lowered to 4.14% and residual density on atom H15 disappeared. The gradual decrease of minimum, maximum and root-mean-square Fourier residual electron density in the unit cell is illustrated in Table 2. The modelling of anharmonicity and of disorder appear to be both necessary to achieve satisfactory *R* factors and residual peaks. The diffraction data and the

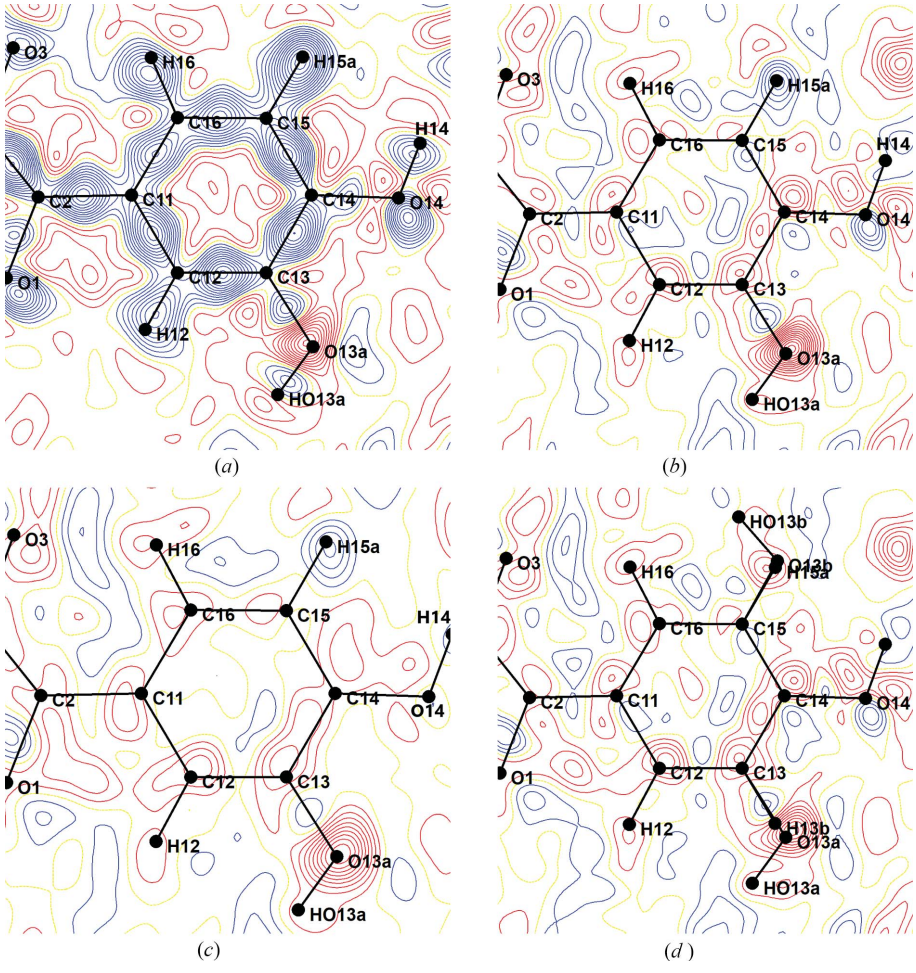

Figure 3
Fourier residual electron density truncated at $s < 0.7$ Å^{-1} reciprocal resolution in the pane of the disordered catechol ring at different steps of the charge density refinement: (*a*) spherical atom model, (*b*) multipolar atom model, (*c*) anharmonicity modelling and (*d*) anharmonicity and disorder modelling.

Table 2
R factor and Fourier residual electron density statistics for different refinement models.

SPH/MUL: spherical/multipolar atom model, ANH: anharmonicity, DIS: disorder modelling.

Model	wR^2I (%)	Min $\Delta\rho$	Max $\Delta\rho_0$	r.m.s. $\Delta\rho$
SPH	6.75	−0.88	1.39	0.109
MUL	5.15	−1.08	1.12	0.088
MUL ANH	4.60	−0.63	1.11	0.086
MUL DIS	5.04	−1.14	0.76	0.087
MUL ANH DIS	4.14	−0.56	0.35	0.066

molecular model are of good quality as shown by the quasi symmetric parabolic shape of the distribution of fractal dimension (Meindl & Henn, 2008) with a flatness $\Delta\rho_0$ at 0.82 e Å^{-3} (Fig. S1). The careful modelling of the disorder and of the anharmonic thermal motion enabled us to decrease the *R* factors and the height of Fourier residual peaks (min and max at −0.56 and 0.35 e Å^{-3}). The unmerged diffraction data sets are included in the supplementary materials. We acknowledge though that archiving of raw diffraction images (not available anymore) would allow a more complete reuse of the data underpinning a study via different processing software.

3.2. Molecular structure and crystal packing

The crystal structure contains no 1-propanol solvent molecule but water which may already be present in the stored sample and/or originate from the ambient air during the slow evaporation from the solvent. The molecular structure of quercetin at ultralow-temperature (20 K) with thermal displacement ellipsoids and atomic labelling scheme is shown in Fig. 2. In the present study, quercetin crystallized as a dihydrate in the triclinic space group $P\overline{1}$ as in its first structural analysis (Rossi *et al.*, 1986; Jin *et al.*, 1990). As is clear from Fig. 2, the benzopyran moiety displays intramolecular hydrogen bonding between the hydroxyl group at C5 position and the carbonyl O atom at C4 position. There is also a C—H···O weak intramolecular interaction between C16—H16 of the catechol ring and the hydroxyl O3 atom. The catechol ring system exhibits conformational disorder over two positions with relative occupancies of 98.4/1.6% in *anti*/*syn* conformation, respectively. This disorder, already suspected (Leopoldini *et al.*, 2004) and visible in the present structure derived from ultrahigh-resolution X-ray diffraction data collected at ultralow temperature, reveals the coexistence of the *anti* and *syn* conformer of quercetin in the condensed phase. This provides an opportunity to understand why the *anti* conformation of quercetin crystallizes in the dihydrate form while the monohydrate form is in the *syn* conformation. Indeed, the intermolecular interactions between the network of water molecules and the disordered catechol ring systems can be compared. It reveals strong hydrogen bonds between the water molecules and the two phenol moieties of the catechol cycle in the *anti* position, in which the phenol oxygen atoms are both hydrogen-bond donors and acceptors (Fig. 4).

This network of hydrogen bonds is a major driving force in crystal packing stabilization of the *anti* conformation. The very high occupancy of the *anti* conformation in this crystal structure indicates that the *anti* conformer with the network of two water molecules is the preferential packing motif relative to the *syn* conformer dihydrate crystal. On the other hand, for the *syn* conformer, a too short intermolecular contact O13*b*···O*W*2 = 2.40 Å would appear in the catechol ring if the water molecule O*W*2 was fully occupied. From a steric point of view, the emergence of the *syn* conformation is less favoured in this environment. The *syn* conformer is compatible only with the O*W*3 water molecule, therefore, the O*W*2 water molecule was modelled with partial occupancy. Moreover, although this crystal structure is affected by conformational disorder, the major component, *i.e.* the *anti* conformer, exhibits geometrical parameters similar to those found by Jin *et al.* (1990) for the same dihydrate crystal. Major distinction lies only in the H atom positions, which in the present structure are constrained at neutron bond length values (Allen & Bruno, 2010). Fig. 5 shows this agreement in the overlay of the two geometries.

In the crystal packing, the intermolecular hydrogen bond network between the guest water molecules and the quercetin

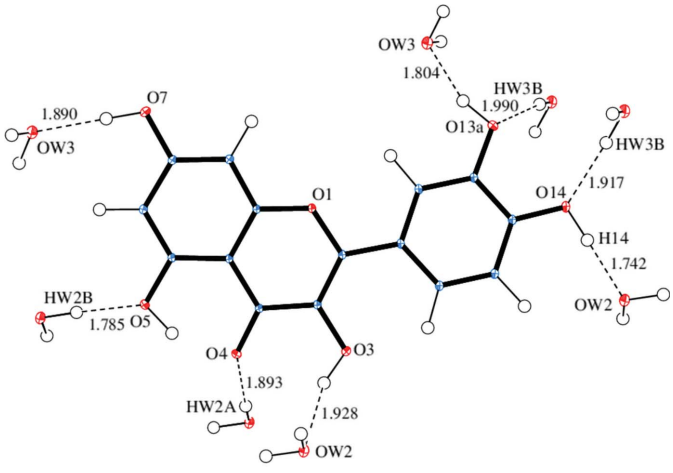

Figure 4
Part of the crystal packing showing hydrogen bonds (black dashed lines) between the quercetin phenol atoms and surrounding water molecules (*anti* conformer, major disorder component).

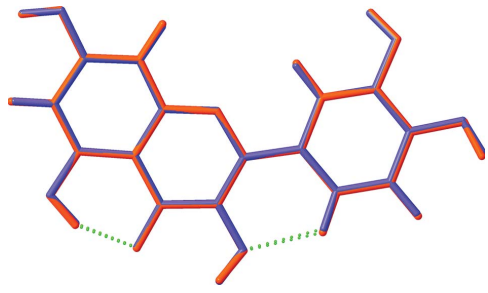

Figure 5
An overlay diagram of the major component (*anti* conformation) of the present crystal structure (red) with that of the Jin *et al.* (1990) study (blue). Green small dots represent intramolecular hydrogen bonds.

Table 3
Topological properties at the critical points of hydrogen bonds for the *anti* main conformation of quercetin.

	$d_{O\cdots H}$ (Å)	d_{1cp} (Å)	d_{2cp} (Å)	ρ_{cp} (e Å^{-3})	$\nabla^2\rho_{cp}$ (e Å^{-3})
O4···H5—O5	1.6882	1.1207	0.5870	0.25	4.62
O4···H5—O5^{i}†	2.6487	1.43	1.3434	0.06	0.96
O3···H16—C16†	2.1132	1.2474	0.8932	0.15	2.20
O5···H*W2A*	2.6116	1.5417	1.1777	0.03	0.68
O5···H*W2B*^{ii}	1.7854	1.172	0.6134	0.20	3.19
O4···H*W2A*^{i}	1.8927	1.2234	0.6694	0.15	2. 47
O14···H*W3A*^{iii}	1.9167	1.2411	0.6756	0.14	2.30
O13*a*···H*W3B*^{iv}	1.9896	1.2794	0.7102	0.12	1.97
O14—H14···O*W2*^{iii}	1.7416	0.5471	1.1949	0.15	4.95
O13*a*—HO13*a*···O*W3*^{v}	1.8037	0.5988	1.2357	0.12	3.82
O7—H7···O*W3*^{ii}	1.8898	0.6221	1.2685	0.11	3.40
O3—H3···O*W2*^{vi}	1.9281	0.6805	1.2976	0.09	2.65
C15—H15*a*···O*W2*^{iii}†	2.4490	1.0620	1.4226	0.06	0.97
C6—H6···O*W3*^{ii}†	2.5319	1.0867	1.4918	0.05	0.80

Symmetry codes: (i) $-x+1, -y+1, -z+1$; (ii) $x-1, y, z$; (iii) $x+1, y-1, z$; (iv) $x, y-1, z$; (v) $-x+2, -y+1, -z$; (vi) $-x+2, -y+1, -z+1$. † C—H···O hydrogen bonds.

host molecule (Table 3), strongly establishes the crystalline cohesion. The quercetin molecules also display parallel stacking contacts between neighbouring molecules related by translation along a = 3.724 Å axis. The distance between two benzopyran mean planes is, for instance, 3.42 Å and the parallel displacement is 1.47 Å. The stacking contacts take place either between benzopyran fragments or between catechol moieties. The distance between mean planes of the catechol portions is 3.40 Å. The stacks thus formed combine with other stacks through hydrogen bonds generated by guest water molecules to form chains parallel to the b axis (Fig. 6).

3.3. Hirshfeld surface analysis and contact enrichment ratios

The Hirshfeld surface around the quercetin molecule (Fig. 7) is coloured according to the normalized contact distance (d_{norm}) (Spackman & Byrom, 1997; McKinnon *et al.*, 1998), which assumes values in the range −0.68 to 1.03.

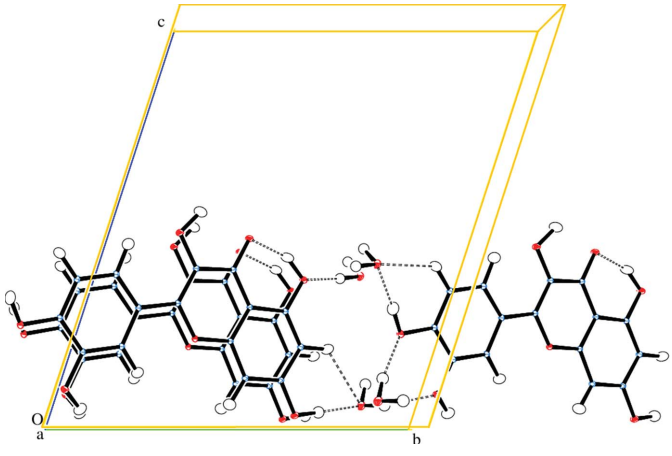

Figure 6
ORTEP view along the short a axis of the partial crystal packing, showing the stacking of the quercetin host molecules, with hydrogen bonds between water molecules and host molecules (dashed lines). For clarity, the minor component of the disordered moiety has been omitted.

Negative d_{norm} values correspond to contacts which are shorter than the sum of van der Waals radii. The colour coding shows the different intermolecular interactions. The red circular regions indicate the strong O—H···O hydrogen bonds whereas the diffuse white patches on the sides near H atoms represent C—H···O, C—H···C weak interactions and H···H (C—H···H—C, C—H···H—O and O—H···H—O) close contacts. The large diffuse white region around chromen-4-one and the catechol ring systems corresponds to aromatic stacking contacts.

The contribution of each interaction type is given the fingerprint plots. As shown in Fig. 8, the largest contribution (38.4%) is from the O···H interactions and are pinpointed by two keen spikes directed toward short distances. The H···H close contacts occupy the second rank and contribute up to 27.5%, whilst the C···C and H···C contacts which correspond to stacking and H···π interactions participate, at 16.3% and 10.4%, respectively. The C···O contacts at 6.2% have a smaller contribution to the crystal packing compared to the others mentioned above whereas the unfavourable O···O contacts are almost absent (1.2%) in the crystal packing.

The fingerprint plots for the *syn* conformation are shown in Fig. S2. While the plots are generally similar to that of the *anti* crystal packing, a difference is found for the shortest H···H

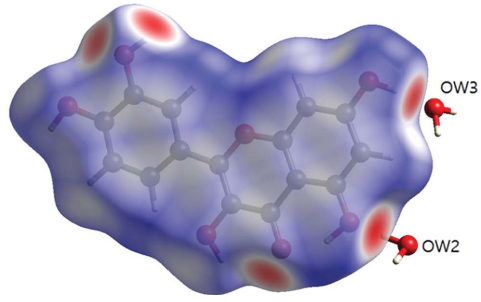

Figure 7
Hirshfeld surface around the quercetin molecule (major disorder component) in the dihydrate crystal form coloured according to d_{norm}, which assumes values in the range −0.68 (H bond region in red) to +1.03.

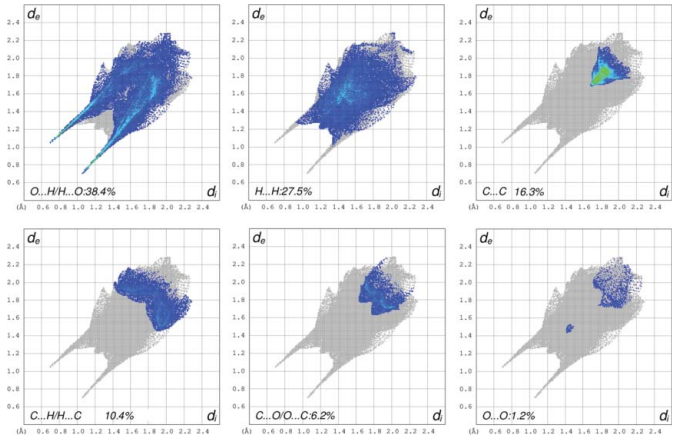

Figure 8
Fingerprint plot for individual interactions around the Hirshfeld surface of quercetin molecule (main conformation) in its dihydrate crystal form.

contacts which are about 2.4/2.1 Å in the *anti*/*syn* conformers, respectively. The shortest distance of 2.104 Å corresponds to the HO13*b*···H16 ($3 - x$, $-y$, $1 - z$) interaction for the *syn* crystal.

The Hirshfeld surface study, in conjunction with contact enrichment ratios analysis, constitutes a powerful and effective tool in scrutiny and quantification of the interactions that occur between molecular entities. We have scrutinized the nature of intermolecular interactions for the *anti* conformer with a network of two water molecules. For the *syn* conformer, only the guest water molecule *W*3 only is compatible with the crystal environment and does not form steric clashes. As shown in Table 4, the polar O···H(—O) contacts with the large contact area at 22.8% in the *anti* conformer (22.4% for the *syn* form) are quite enriched at E = 2.20 (E = 1.88 for the *syn* form). In the dihydrate form, these contacts correspond to the strong hydrogen-bonding network which is established between the *anti* conformation of the quercetin molecule and the two guest water molecules. The oxygen atoms of quercetin are acceptors in four hydrogen bonds and the phenol hydrogen atoms are involved in four hydrogen bonds (Fig. 4). As for the *syn* conformation, the O···H—O enrichment ratio is slightly lower than for the *anti* form and results from the smaller number of such polar interactions which form between the host conformer and the *W*3 water guest moiety (Fig. S3).

The C···C contacts are the most abundant type in both conformations, representing 27.1%/25.8% of the interaction surface for the *anti*/*syn* conformers, respectively, and constitute one of the most over-represented contacts with enrichment ratios of 2.02/2.09, respectively. This enrichment highlights the extent of parallel displaced (translation along **a** axis) aromatic stacking stabilizing the crystal packing of quercetin dihydrate. In general, in heterocyclic compounds, this contact type is privileged because of the possibility to form favourable electrostatic complementary orientations of molecules in the crystal packing (Jelsch *et al.*, 2014; Martinez & Iverson, 2012).

The hydrophobic H(—C) atoms occupy the smallest proportion on the Hirshfeld surface (S_{ext} = 16.8/12.6% for the *anti*/*syn* conformation) compared with the C, O and H(—O) atom types which are all greater than 23%. The H(—C) atoms exhibit H(—C)···H(—C) self-contacts and O···H(—C) weak hydrogen bonds, both of which are slightly enriched [$E_{H(-C)\cdots H(-C)}$ = 1.57/1.13 and $E_{O\cdots H(-C)}$ = 1.61/1.31]. These two types of contacts, although favoured, occur with small contact surfaces (5.0/2.7% and 13.8/10.7%, respectively). Compared with O···H—O and C···C, they can be classified as second-order interactions in the hierarchy of crystal stabilizing forces.

As for the other contacts, whose enrichment ratios are less than unity, these are qualified as disfavored contacts and are often destabilizing interactions. Indeed, due to the electrostatic repulsive nature, homo-contacts involving charged atoms, are generally avoided in molecular crystals. This is the case for H(—O)···H(—O) and O···O contacts in the present crystal structure.

The packing of the *anti* and *syn* form of the quercetin hydrate can also be analysed in terms of hydrophilic and hydrophobic interactions (Table 4). The hydrophobic contacts (involving C and H(—C) atoms) in the both conformation are globally enriched at E = +1.27. Due to the propensity of heterocyclic compounds to form stacking contacts rather than C—H···π weak hydrogen bonds, C···C contact appears as one of the most enriched (E = 2.02/2.09) while C···H(—C) weak hydrogen bonds are significantly under-represented (E = 0.43/0.38).

Table 4
Nature of intermolecular contacts on the Hirshfeld surface around the quercetin molecule by chemical types.

The first row and first column indicate the chemical species involved in the contacts. The second row shows the atom surfaces related to the atom types that are indicated in the first row. The percentage of actual contact types C_{xy} between chemical species is then given followed by the enrichment ratios E_{xy}. The reciprocal contacts $X\cdots Y$ and $Y\cdots X$ have been merged. The major contacts as well as the most enriched ones are highlighted in bold. The hydrophobic hydrogen atoms bound to carbon [H(—C)] are distinguished from the polar H atoms bound to oxygen [H(—O]. For the major *anti* conformation of quercetin, the two water molecules were included in the environment . For the major *anti* conformation of quercetin, the two water molecules were included in the environment H(—O) (first entry). For the *syn* conformation, the calculation was done with only the H*W*3*A*—O*W*3—H*W*3*B* molecule (second entry in italics). The atoms were grouped in hydrophobic [H(—C) and C] and hydrophilic [H(—O) and O] atoms.

Atom	O	H(—O)	H(—C)	C
% surface quer	24.9/*25.1*	18.0/*19.5*	19.0/*19.2*	38.1/*36.3*
% surface ext	23.2/*26.3*	24.8/*27.1*	16.8/*12.6*	35.2/*34.0*
		% actual contacts		
O	1.63/*5.27*			
H(—O)	**22.8/*22.4***	4.2/*3.0*		
H(—C)	**13.8/*10.7***	6.3/***11.4***	5.0/*2.7*	
C	8.2/*7.7*	5.3/*6.7*	5.6/*4.2*	**27.1/*25.8***
		Enrichment		
O	0.28/*0.80*			
H(—O)	**2.20/*1.88***	0.93/*0.56*		
H(—C)	**1.61/*1.31***	0.82/***1.50***	**1.57/*1.13***	
C	0.47/*0.43*	0.34/*0.41*	0.43/*0.38*	**2.02/*2.09***
	Hydrophilic	Hydrophobic	Hydrophilic/Hydrophobic	
% surface quer	42.9/*44.6*	57.1/*55.4*		
% surface ext	48.0/*53.3*	52.0/*46.7*		
% contacts	28.6/*30.7*	37.7/*32.8*	33.7/*36.6*	
Enrichment	1.39/*1.29*	1.27/*1.27*	0.68/*0.73*	

The enrichment was also computed by grouping hydrophilic [O and H(—O)] and hydrophobic [C and H(—C)] atom types (bottom of Table 4). Globally, hydrophilic contacts (involving O and/or H(—O) atoms) are over-represented at E = 1.39/1.29 for the *anti*/*syn* forms, respectively. The hydrophobic contacts are also enriched and are mostly of C···C type, resulting from the aromatic stacking. In both conformations, the formation of hydrophilic and hydrophobic contacts with similar propensities highlights the amphipathic character of the quercetin hydrate crystal packing. Hydrophilic/hydrophobic mixed contacts, although second in terms of contact area (33.7/36.6%) and despite the occurrence of moderately favoured weak hydrogen bonds of type C—H···O are globally significantly disfavoured in the dihydrate and monohydrate forms at E = 0.68/0.73, respectively

Quantitative investigation of intermolecular interactions of the *anti* and *syn* conformers of quercetin in the dihydrate and monohydrate crystal packings *via* analysis of intermolecular contacts enrichments presents common trends. The

O···H(−O) strong hydrogen bonds and consequently the hydrophilic/hydrophilic contacts appear however more favoured in the *anti* conformation which is richer in hydrophilic groups. This obviously confirms the affinity of the *anti* conformer for the dihydrate network.

3.4. Charge density distribution

In this work, due to the presence of disorder, some constraints were applied during the refinement. The minor component has only 1.6% occupancy and its charge density was constrained to be identical to that of the major component of the catechol moiety. Despite the defiance caused by the disorder in the crystal structure, the refinement with constraints made it possible to access a meaningful multipolar model. Topological analysis of the charge density provides valuable information on the nature of chemical bonds and on both intra- and intermolecular interactions. Hence, the topological analysis is performed on a model with the major disorder component *i.e.* the *anti* conformation at 100% occupancy.

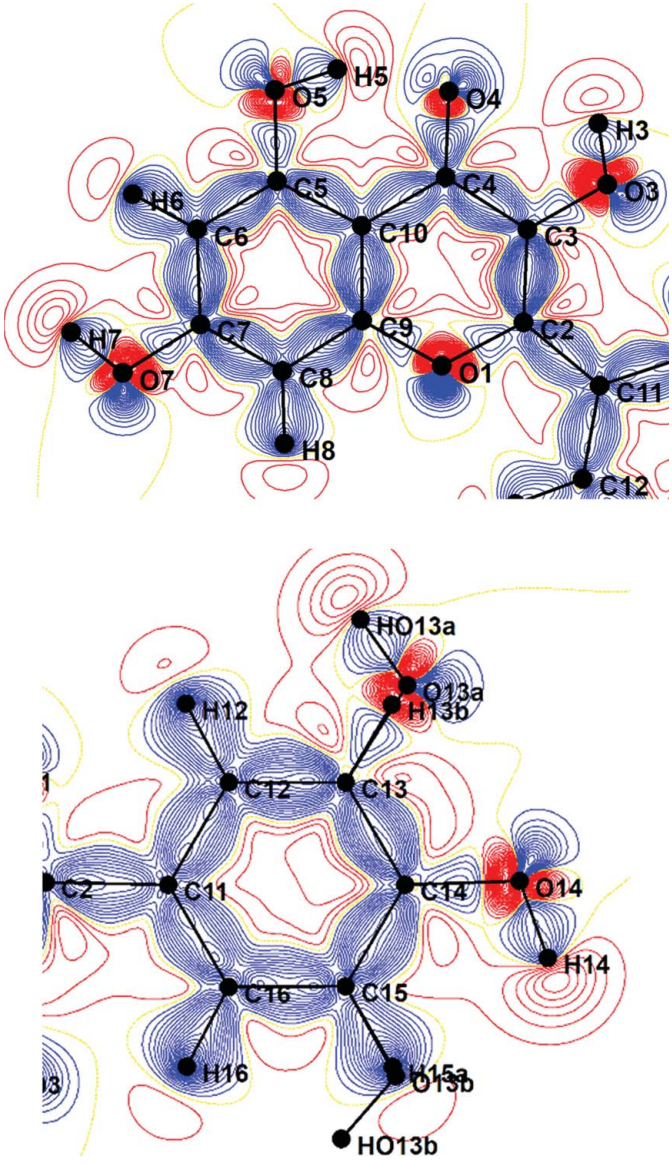

Figure 9
Static deformation electron density maps from experimental charge density. Contour intervals are 0.05 e Å^{-3}. Blue lines represent positive contours, red lines are negative contours and the yellow lines zero contours. (*a*) In the chromen-4-one plane and (*b*) in the phenyl plane of catechol ring.

The deformation density maps in the planes of the chromen-4-one and the catechol rings are displayed in Fig. 9. This picture shows the aspherical charge density distribution in various types of bonds and regions of the quercetin molecule. Thus, one observes that the bonding electron density peaks of the C—C homoatomic bonds are located at middle points whilst for the C—O and O—H heteroatomic bonds they are moved away from the O atoms. These observations are further supported by the molecular graph given in the supplementary information (Fig. S4) in which the (3, −1) covalent bond critical point positions are shown. The critical point positions reveal the polarity of the bond. Indeed, on a covalent bond, the critical point is placed closer to the atom whose partial atomic charge tends to have a positive value. The electron lone pairs of all oxygen atoms as well as the electron depletions near the hydrogen atoms in the C—H and O—H bonds reveal the polar nature of atoms, which are highlighted in Fig. 9.

The deformation density maps of the O1 ether atom and of the non-disordered phenol groups is shown in Fig. 10 in the electron lone pairs (LPs) plane. As expected, the two lone pairs appear as a lobe with only one maximum for the ether oxygen atom located on an aromatic ring chromen-4-one. This is in accordance to previous observation (Ahmed, Jelsch *et al.*, 2013) that ether groups involving sp^2 carbon atoms show merged lone pairs, in contrast to ether groups formed by sp^3C atoms which have distinct lone pairs peaks. Phenol oxygen atoms show two distinct LPs lobes in the deformation electron density maps, but the two LPs are slightly closer compared to alcohol groups (Ahmed, Jelsch *et al.*, 2013). The LPs of phenol oxygen atoms often appears smeared and merged from our experience in building the ELMAM2 electron density database (Domagala *et al.*, 2012) with diffraction data measured at 100 K. This is due to the significant thermal motion of the phenol oxygen atoms in the direction of the two LPs which is perpendicular to the aromatic cycle. Moreover, as the LPs are very close to each other and to the nucleus ($d \sim 0.3$ Å), they require ultrahigh resolution to be well refined and observed. In the present charge density study at 20 K such thermal

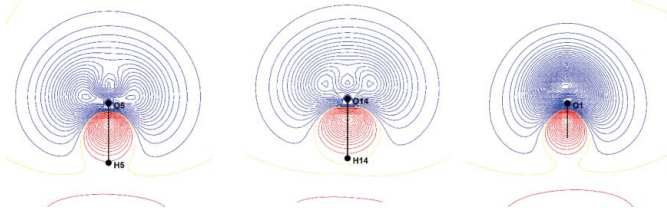

Figure 10
Static deformation electron density in the lone pairs plane for the O5 and O14 phenol and the O1 ether oxygen atoms. Contours as in Fig. 9.

Table 5
Topological properties of total electron density at (3, −1) critical points (cp) of covalent bonds of the major disorder component and water molecules of quercetin dihydrate.

d_{12} is the interatomic distance; d_{1cp} and d_{2cp} (Å) are the distances between the first/second atom and the cp; $\rho(\mathbf{r}_{cp})$ is the electron density (e Å^{-3}); $\nabla^{2,}\rho_{CP}$ is the Laplacian (e Å^{-5}); λ_1, λ_2 and λ_3 are the eigenvalues of the Hessian matrix (e Å^{-5}); ε is the ellipticity.

Bonds	d_{12}	d_{1cp}	d_{2cp}	ρ	$\nabla^2\rho$	λ_1	λ_2	λ_3	ε
O4—C4	1.2714	0.7957	0.4757	2.46	−27.10	−22.20	−19.20	14.30	0.16
O1—C2	1.3693	0.8076	0.5617	1.91	−11.90	−14.10	−13.10	15.30	0.08
O1—C9	1.3582	0.8198	0.5386	1.92	−14.70	−15.20	−13.20	13.70	0.15
O3—C3	1.3578	0.8105	0.5475	1.94	−12.80	−14.50	−13.30	14.90	0.09
O5—C5	1.3527	0.8109	0.5417	1.99	−14.60	−15.40	−13.90	14.70	0.10
O7—C7	1.3545	0.8115	0.5431	1.97	−15.10	−14.90	−14.30	14.20	0.05
O13*a*—C13	1.3724	0.8243	0.5482	1.88	−13.60	−14.50	−13.70	14.70	0.06
O14—C14	1.3645	0.8186	0.5460	1.95	−13.80	−14.90	−13.80	14.90	0.08
C2—C3	1.3820	0.6905	0.6916	2.24	−20.20	−19.00	−13.20	12.00	0.44
C3—C4	1.4383	0.7089	0.7296	1.96	−15.30	−15.60	−12.00	12.40	0.30
C4—C10	1.4353	0.7353	0.7001	1.85	−12.80	−14.20	−11.30	12.60	0.27
C5—C6	1.3827	0.7111	0.6716	2.06	−16.40	−16.30	−12.40	12.30	0.32
C5—C10	1.4190	0.7265	0.6926	1.96	−14.40	−15.10	−11.70	12.40	0.28
C6—C7	1.4115	0.6831	0.7287	2.05	−15.90	−16.20	−12.70	13.00	0.28
C7—C8	1.3995	0.7261	0.6736	2.05	−15.70	−16.00	−12.40	12.80	0.29
C8—C9	1.3976	0.6569	0.7407	2.03	−15.50	−15.90	−12.10	12.50	0.31
C9—C10	1.4041	0.7292	0.6750	2.09	−17.20	−16.70	−13.00	12.50	0.28
C2—C11	1.4642	0.7477	0.7166	1.82	−11.60	−13.70	−10.90	13.10	0.26
C11—C12	1.4171	0.7107	0.7065	1.96	−13.10	−14.80	−12.40	14.20	0.20
C11—C16	1.4133	0.7065	0.7068	1.98	−13.70	−15.10	−12.70	14.10	0.19
C12—C13	1.3913	0.6853	0.7061	2.16	−17.30	−17.10	−13.40	13.20	0.28
C13—C14	1.4113	0.6979	0.7135	2.10	−17.90	−17.10	−12.80	11.90	0.33
C14—C15	1.4011	0.6960	0.7052	2.08	−16.50	−16.60	−13.00	13.10	0.27
C15—C16	1.3915	0.6962	0.6954	2.03	−14.40	−15.70	−13.00	14.30	0.21
O3—H3	0.9721	0.7473	0.2248	2.19	−31.40	−34.30	−34.20	37.00	
O5—H5	0.9720	0.7452	0.2268	2.12	−24.10	−32.20	−32.10	40.10	
O7—H7	0.9767	0.7447	0.2320	2.16	−26.20	−32.50	−32.50	38.70	
O13*a*—HO13*a*	0.9826	0.7597	0.2229	2.09	−30.40	−33.10	−32.90	35.60	0.01
O14—H14	0.9782	0.7564	0.2218	2.10	−29.30	−33.10	−33.00	36.90	0.01
C6—H6	1.0815	0.7126	0.3689	1.76	−15.00	−16.40	−15.60	17.10	0.05
C8—H8	1.0743	0.7121	0.3622	1.79	−15.60	−16.50	−16.50	17.40	0.00
C12—H12	1.0677	0.6892	0.3786	1.87	−16.60	−17.30	−16.80	17.40	0.03
C15—H15*a*	1.1105	0.7026	0.4079	1.69	−13.00	−14.90	−14.40	16.40	0.04
C16—H16	1.0718	0.6866	0.3852	1.90	−16.90	−17.70	−16.90	17.70	0.05

displacement is limited (Fig. 2), the largest U_{ij} tensor eigenvalue is in the 0.0146–0.156 Å^2 range for all four non-disordered phenol oxygen atoms, which corresponds to a root mean square displacement lower than 0.125 Å.

The topological properties of electron density evaluated by QTAIM analysis (Bader, 1990) are listed in Table 5. The electron density $\rho(\mathbf{r}_{cp})$ at the critical points of the C—C bonds of the chromen-4-one ring and of the catechol moiety stand the ranges from 1.85 to 2.24 e Å^{-3} and 1.96 to 2.16 e Å^{-3}, respectively. The average $\rho(\mathbf{r}_{cp})$ values of the C—C bonds in the two aromatic rings are almost equal (2.03 e Å^{-3} and 2.05 e Å^{-3}, respectively). The C2—C11 single bond which serves as linker between the chromen-4-one ring and of the catechol cycle exhibits a weaker electron density value at $\rho(\mathbf{r}_{cp})$ = 1.82 *e*Å^{-3} compared to the C—C aromatic bonds in the quercetin molecule. The ether C—O bonds exhibit critical point electron density values at 1.91 and 1.92 e Å^{-3} which are in the same range as those observed in the chromen-2-one ring of the Coumarin-102 dye (Bibila Mayaya Bisseyou *et al.*, 2012). As for the phenol C—O bonds, the electron density $\rho(\mathbf{r}_{cp})$ values range between 1.88 and 1.99 eÅ^{-3} with average value of ∼1.95 e Å^{-3}. This value is similar to that reported for the same bond type (1.94 e Å^{-3}) for the paracetamol molecule (Bouhmaida *et al.*, 2009). The carbonyl C4═O4 bond has a higher electron density at $\rho(\mathbf{r}_{cp})$ = 2.46 e Å^{-3}. This significantly higher electron density compared to those of the ether and phenol C—O bonds highlights the double bond character of the C4═O4 bond. However, this value is slightly lower to that reported for the carbonyl bond of the chromen-2-one ring (2.96 e Å^{-3}) of the Coumarin-102. On the hydroxyl O—H phenol bonds, the $\rho(\mathbf{r}_{cp})$ values at the bond critical points vary from 2.09 to 2.19 *e*Å^{-3} and are very close to the value found in paracetamol by Bouhmaida *et al.* (2009). The C—H bond have electron density values comparable with those reported for aromatic scaffold (Ahmed, Yar *et al.*, 2013; Rajalakshmi *et al.*, 2014).

3.5. Laplacian and ellipticity on bond critical points

The Laplacian $\nabla^2\rho$ of electron density and ellipticity at the bond critical point (cp) are useful and powerful descriptors that allow to characterize a chemical bond type and an interaction between two atoms. The negative $\nabla^2\rho$ value at the bond cp means that electronic charges are locally concentrated there and the chemical bond formed is a shared-shell interaction, *i.e.* a covalent bond. The charge depletion or

closed-shell interaction is materialized by positive value of Laplacian at the bond cp. Inspection of Table 5 reveals that all $\nabla^2\rho$ values of the Laplacian at the bond cp are negative and are within the typical ranges for each bond type. Thus the $\nabla^2\rho$ of the C—C bonds of the chromen-4-one and catechol rings exhibit average values which are almost identical (−15.9 and −15.5 e Å^{-5}, respectively). Based on $\nabla^2\rho$ values, one can note that the C2—C11 bond is the weakest C—C bond with $\nabla^2\rho$ value at −11.6 e Å^{-5} and is presumably the only single C—C bond in the quercetin molecule. However, analysis of ellipticity values (0.19 to 0.44) show that all C—C bonds present ellipticity magnitudes consistent with their partial double-bond character. This result emphasizes the existence of electron delocalization in both chromen-4-one and catechol cycles which is at the basis of the charge transfer between both moieties within the quercetin molecule *via* the C2—C11 bond as suggested in numerous theoretical studies (Zheng *et al.*, 2017; Torres *et al.*, 2011; Li *et al.*, 2020). Otherwise as expected, there is a significant difference between the $\nabla^2\rho_{cp}$ values at the carbonyl C4═O4 bond and at the ether and phenol C—O bonds. The strong negative $\nabla^2\rho_{cp}$ value at the carbonyl C4═O4 bond (−27.1 e Å^{-5}) indicates that the electron density is much more concentrated there compared to the ether and phenol C—O bonds and clearly indicates the double bond character of this bond. This observation is confirmed by the higher ellipticity value of the carbonyl bond (0.16 versus 0.08 and 0.15, respectively). We also note that the electron densities are quite concentrated at bond cp of the O—H phenol groups, as the negative Laplacian values are large in magnitude, comprised between −24.1 and −31.4 e Å^{-5}.

The $\nabla^2\rho_{cp}$ value of C—H bonds varies between −13.0 and −16.9 e Å^{-5}, the average value being at −15.4 e Å^{-5} which is slightly smaller in magnitude than the value of −18.1 e Å^{-5} reported by Rajalakshmi *et al.* (2014) on pyrazinamide. Interestingly the ellipticities of the bonds involving H atoms are very low or even null, this denotes their single bond character.

3.6. Electrostatic complementarity on the Hirshfeld surface

The electrostatic potentials (ESP) generated by a molecule and by a cluster of surrounding molecules can be computed on

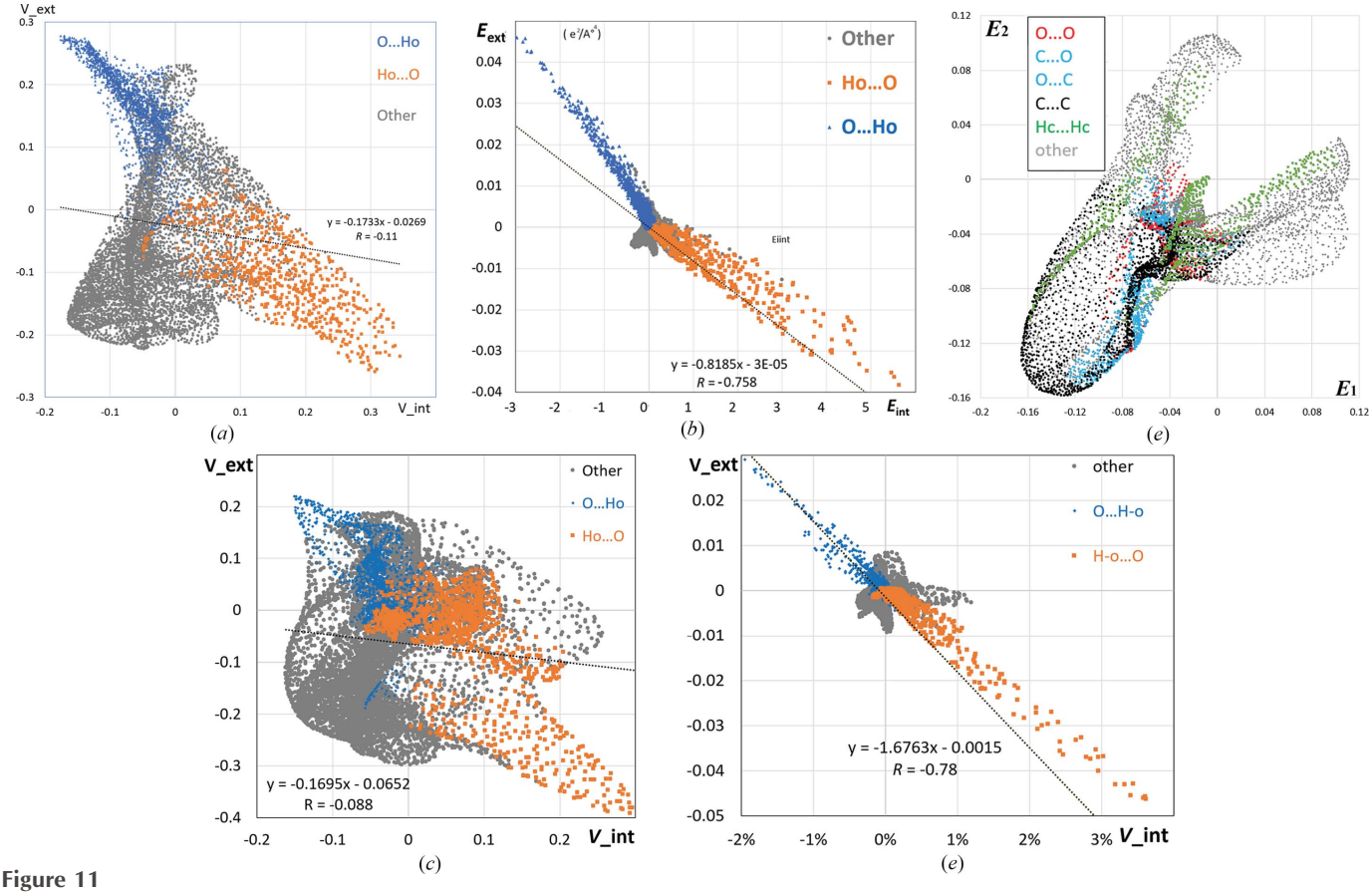

Figure 11
(*a*) Scatterplot of deformation electrostatic potential values on the Hirshfeld surface around the *anti* quercetin molecule. $V_{def-querc}$ is generated by the quercetin molecule and $V_{def-ext}$ is generated by a cluster of surrounding molecules. The units are in e Å^{-1}. (*b*) E_{def} corresponds to the electrostatic energy density resulting from the product between V_{def} and the ρ, the total electron density generated by the quercetin molecule on the Hirshfeld surface. The units are in e^2 Å^{-4}. The minor disorder was removed and occupancy factors set to unity for these calculations. The contact points related to strong O···H—O hydrogen bonds are highlighted in colour. The contact type is indexed according to the closest atom inside and outside of the Hirshfeld surface. (*c*) The scatterplot of V_{def} on the Hirshfeld interface between two stacking quercetin molecules related by translation **a**. The Hirshfeld interface between the two molecules was limited to electron density values $\rho > 0.0013$ e Å^{-1} and some contact types are highlighted in colour. (*d*) Scatterplot of V_{def} in the *syn* crystal packing. (*e*) Scatterplot of E_{def} in the *syn* crystal packing.

Table 6
Electrostatic energies (kJ mol^{-1}) of $Q\cdots Q$ and $Q\cdots$water dimers in the crystal packings of both conformers.

ORTEP symmetry 51 corresponds to the inversion. Reciprocal symmetry dimers are regrouped.

Dimer	Symmetry	*anti*	*syn*
$Q\cdots Q$	36501 and 74501	−8.3	−6.6
	46501 and 64501	−13.4	−12.3
	45501 and 65501	0.7	−4.4
	66551	4.1	−8.5
	66651	−2.9	−2.7
	75651	3.5	−75.0
	76551	12.6	3.5
	85551	−10.3	−0.0
	85651	−2.4	−41.1
	Sum	−16.6	−147.2
$Q\cdots W2$	45501	−43.7	
	54501	7.0	
	55501	−8.0	
	64501	−70.6	
	66651	−19.6	
	76651	−34.3	
	Sum	−169.3	
$Q\cdots W3$	45501	−54.7	−53.8
	54501	−23.2	−9.8
	64501	−30.1	−22.3
	76551	2.7	−3.9
	77551	−0.7	−0.6
	86551	−2.8	−0.5
	Sum	−108.9	−90.9
Global	Sum	**−344.7**	**−213.94**

the Hirshfeld surface to illustrate the electrostatic complementarity of the molecule with its crystal packing environment (Spackman *et al.*, 2008; Jelsch *et al.*, 2020, Fig. 11, Fig. S5). The deformation of the ESP V_{def}, which is directly derived from the deformation electron density ρ_{def} was computed, as it represents more balanced electropositive and electronegative values than the total potential which takes overwhelmingly positive values on the Hirshfeld surface for short contacts. The scatterplots (V_{def_int},) for the *anti*/*syn* conformations show only a very modest anticorrelation r = −0.1/−0.088 of the inner and outer electrostatic potential values [Figs. 11(*a*) and 11(*d*)]. There are indeed electropositive regions interacting, through O—H···O hydrogen bonds, with electronegative regions and vice versa. The *syn*/*anti* graphs show some similarity and some differences as the hydrogen bond interactions differ in the two cases. The *anti* crystal packing has more pronounced O···H(—O) interactions as there is an additional water molecule. There are however also some regions with negative inner ESP interacting with regions yielding electronegative exterior ESP, around C2—O1 above the C_5O heterocycle (Figs. S5a and S5b). This electronegative region on the quercetin surface appears more neutral when the ESP is derived from the ELMAM2 database (Domagała *et al.*, 2012) transferred electron density (Fig. S5c). The ESRF and ELMAM2 ESPs show globally a correlation coefficient of 82% on the Hirshfeld surface (Fig. S5d).

The E_{def} complementarity scatterplots, where the electrostatic energy density E_{def} is obtained by the product between V_{def} and ρ, the total electron density generated by the inner molecule, have been described by Jelsch *et al.* (2023). It should be remembered that on the Hirshfeld surface $\rho_{int}(\mathbf{r}) = \rho_{ext}(\mathbf{r})$. The E_{def} fingerprint of interactions corresponds to a V_{def} scatterplot where the values are weighted by the electron density ρ; it gives more weight to the strong interactions at short distance which display largest ρ values. On the other hand, weak interactions at long distance (low ρ values) are given less importance and these (E_{def_int},E_{def_ext}) points are shifted towards the origin (0,0).

The unfavourable contacts between electronegative regions appear much less prominent in the scatterplot of electrostatic energy densities [Fig. 11(*b*)]. The strong O···H—O hydrogen bonds appear as spikes in the (E^-, E^+) quadrant while the reciprocal O—H···O interactions appear in the (E^+, E^-) quadrant of Figs. 11(*b*) and 11(*e*). The correlation coefficient between the inner and outer E_{def} values reaches here −0.758/−0.780, suggesting a good electrostatic complementarity at the Hirshfeld surface in both *anti*/*syn* conformations. The graph of the *syn* conformation shows significantly fewer points on the Hirshfeld surface involved in O—H(—O) hydrogen bonds than the *anti* one; the number of O—H···O interactions appears reduced from 11 to 7 in Table S2. The interactions which are attractive from an electrostatic point of view are located in the (E^+, E^-) and (E^-, E^+) quadrants. The repulsive contacts between electronegative atoms appear to have much less importance in the (E^-, E^-) quadrant than in the (V^-, V^-) quadrant. They correspond to weak stacking contacts between two quercetin molecules related by unit cell translation a = 3.724 Å.

The dimer of parallel displaced quercetin molecules does not display good electrostatic complementarity on the Hirshfeld interface. The regions around the O1 ether atom have negative inner and exterior V_{def} values on the Hirshfeld surface and interact with each other on the opposite sides; the O1···O1 distance is actually only 3.724 Å. Fig. 11(*c*) shows the electrostatic potentials generated by each quercetin molecule within a dimer related by ***a*** translation. The contacts with V_{def} values both negative correspond to C···C, C···O and O···O contacts. The stacking between the two molecules shows unfavourable electrostatic complementarity as the two V_{def} values are positively correlated (r = +0.693). The electrostatic energy between two such quercetin molecules in *anti* conformation is actually positive with E_{elec} = +0.68 kJ mol^{-1} showing that the electrostatic contribution is here slightly repulsive. In a cocrystal of gallic acid (also a polyphenol), the electrostatic potential values (V_1, V_2) were found to be correlated in the parallel dimer of gallic acid and anticorrelated in the antiparallel dimer found in the crystal packing (Pal *et al.*, 2022). Geometries resulting from parallel displaced stacking interactions may less likely form contacts with good electrostatic complementarity than other isometries such as rotations axes, inversions or glide planes.

The electrostatic energy (E_{elec}) was also computed between quercetin and all contacting molecules (quercetin or water) in the *syn* and *anti* crystal packings (Table 6). The *syn* crystal structure contains only water molecule *W*3 while the *anti* structure is dihydrate. The E_{elec} values between quercetin and

the whole crystal packing was interpolated from calculations of E_{elec} between quercetin and large clusters of molecules using increasing radius (Table S3, Fig. S6). The scatter graph (E_{elec} versus cluster radius) displays convergence toward large radii ($1/r \rightarrow 0$). One can also see through this graph that more conformational stability is observed for the *anti* form with a significant energy gap over *syn* structure around 130 kJ mol^{-1}. The stronger stability of the *anti* conformer in dihydrate medium results of the more favourable interactions between quercetin and its surrounding molecules, the most stabilizing contributions being quercetin–water dimer interactions. Indeed, the water mediated interactions (water molecules in contact with quercetin) are generally more attractive when they take place in the dihydrate environment. The global E_{elec} energy between quercetin and the six surrounding *W*3 molecules is −108.94 and −90.86 in the *anti* and *syn* forms, respectively. Moreover, the six interactions of quercetin with *W*2 water molecules are absent in the *syn* conformation.

As for quercetin···quercetin dimers, the *anti* form has some weakly attractive dimers and three slightly repulsive ones. On the other hand, the *syn* form display two significantly favourable dimer interactions: $Q\cdots Q(2-x,-y,1-z)$ reaches E_{elec} = −74.97 kJ mol^{-1} whereas $Q\cdots Q(3-x,-y,1-z)$ is at −41.09 kJ mol^{-1}. These dimers are attractive in the *syn* form, as can be seen Fig. S7, because the hydroxyl groups O3—H3 and O13*b*—HO13*b* interact with each other in a favourable antiparallel geometry. This is not the case in the *anti* conformer where, instead, there is a repulsive O3—H3···H15*a*—C15 interaction. The same attractive antiparallel configurations occur in the two *syn* dimers (Fig. S7), as the symmetry related molecules differ by a translation along the short axis *a* = 3.724 Å. The contributions of the two O3—H3···O13*b*—HO13*b* interactions to E_{elec} when only the four atoms are considered are −74.78 and −22.80 kJ mol^{-1} in the (2 − *x*, −*y*, 1 − *z*) and (3 − *x*, −*y*, 1 − *z*) dimers, respectively.

In summary, the stronger electrostatic energy between quercetin and the water molecules in the *anti* crystal is partially counterbalanced in the *syn* crystal packing by two very favourable quercetin···quercetin interactions. The result indicates that the interactions between the *anti* conformer and water molecules have a major contribution in the crystal stabilization and outlines the key role of these guest molecules in formation of the dihydrate quercetin packing. The summation of E_{elec} over the close contacts between quercetin and the surrounding molecules (Table S4) yields a stronger energy for *anti* than for the *syn* conformation (−344.70 and −213.94 kJ mol^{-1}, respectively). This electrostatic energy analysis confirms the favourable balance towards the formation of the *anti* conformation compared to the *syn* one in the quercetin hydrated crystal.

3.7. Topological analysis of hydrogen-bonding interactions

Topological analysis of the electron density on both intra- and intermolecular interactions were performed on the major disorder component, with all occupancy factors set to unity. For these non-covalent contacts, the characteristics of (3, −1) type cps are enclosed in Table 3. The $\rho(\mathbf{r}_{cp})$ electron density takes conventional values which span the interval 0.033 to 0.252 e Å^{-3} and the positive Laplacian values at all cps show their closed-shell interaction character (Gatti, 2005). These non-covalent contacts can be classified into two groups: the O—H···O hydrogen bonds and the weak C—H···O interactions. The electron density value at the bond critical point of the pair of atoms being in contact (H···O) reflects the hydrogen-bond strength (Espinosa *et al.*, 1998; Espinosa & Molins, 2000), this descriptor can be used for an estimation of such strength.

Globally, the values of electron density at critical point for the hydrogen bonds decrease with the interatomic distance as illustrated by the graph in Fig. S8 representing the electron density at the cp as a function of distance between interacting atoms. Thus, the O4···H5—O5 intramolecular hydrogen bond, forming a six- membered ring, appears as the strongest non-covalent interaction as it has the greatest electron density at the cp (ρ_{cp} = 0.252 e Å^{-3}) and also the shortest $d_{O\cdots H}$ distance. Among the intermolecular hydrogen bonds, the O5···H*W*2*B*–O*W*2 interaction is the strongest, according to ρ_{cp} value, followed by the O14—H14···O*W*2, O4···H*W*2*A*–O*W*2 and O14···H*W*3*A*—O*W*3 contacts. The C—H···O intermolecular contact are recognized by weaker ρ_{cp} values which do not exceed 0.060 e Å^{-3}. The intramolecular C16—H16···O3 interaction, forming a six membered ring, has relatively high ρ_{cp} = 0.153 e Å^{-3} value. Interestingly, the O4 carbonyl atom, which is the strongest hydrogen bond acceptor in the quercetin molecule, participates in three hydrogen bonds (both intra- and intermolecular) and forms the strongest one (Table 3).

3.8. Electrostatic interaction energy of quercetin in binding site of hIPMK

The interaction profile of quercetin in the binding site of human inositol polyphosphate multikinase hIPMK protein structure (PDB code 6m89) is summarized in Fig. 12 and the electrostatic interaction energy for all interactions of quercetin with entire protein for this binding mode is −202.5 kJ mol^{-1}. Analysis of individual contribution for each residue of the binding site allows us to quantify interaction types which contribute mostly to the binding affinity of quercetin with the hIPMK target. The highest attractive electrostatic interaction energies are observed for hydrogen bonds formed with Asp68_OD1 and Val69_NH with electrostatic energies E_{elec} of −27.2 and −44.4 kJ mol^{-1}, respectively. However, the energy between quercetin and Glu 67 has a slightly positive E_{elec} energy of 12.1 kJ mol^{-1}, as the attractive hydrogen bond C═O···H—O is counterbalanced by a repulsive C═O···O═C contact. Hydrophobic contact interactions involve residues Ile_1, Val_9, Ile_78, Thr_70, Leu_190 and Ile_205, all with attractive E_{elec} energies not exceeding −12.6 kJ mol^{-1} (Table S4). The presence of water molecules in the binding site (Fig. S9) further strengthens the affinity of quercetin with the hIPMK target. Indeed, the water molecules

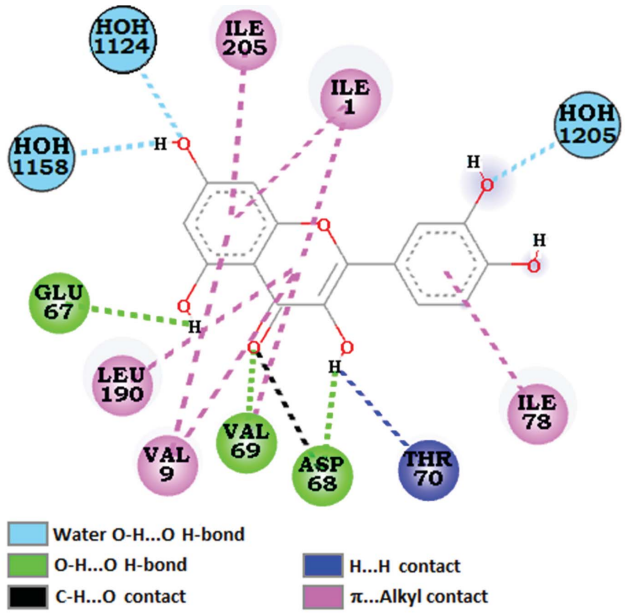

Figure 12
2D scheme of interactions of quercetin with the residues of the binding site hIMPK and three key water molecules.

HOH 1124 and HOH 1158 form strongly attractive hydrogen bonds with quercetin, displaying electrostatic energies of −42.3 and −29.3 kJ mol^{-1}, respectively. The interaction of quercetin with the water molecule HOH 1205 is much lower at −5.9 kJ mol^{-1} due to the proximity of H*W*32 to a neighbour H—O phenol group. When the electrostatic interaction energy is evaluated by ignoring the three water molecules (Fig. S10), its overall value drops to −124.7 kJ mol^{-1}.

Thus, the presence of structural water molecules in the binding site of hIPMK constitute a key factor fuelling the affinity of quercetin for this target and play a role in its inhibition. It is also interesting to note that the quercetin molecule in the hIPMK binding site exhibits an interaction pattern broadly similar to that observed in its dihydrate crystalline environment: O—H···O hydrogen bond interactions at the carbonyl O atom and hydroxyl groups and stacking contacts on the flat faces of the chromen-4-one and catechol ring systems (Fig. 12). However, quantification of the interactions reveals that they are globally stronger in the native crystalline environment of quercetin. Indeed, the electrostatic energies of both conformers within the crystal are more attractive compared to that of quercetin in the hIPMK binding site (see Fig. S4). In addition, quercetin–water interactions are also stronger in the native crystal with electrostatic energy values that reach −59.12 kJ mol^{-1} and −58.42 kJ mol^{-1}, respectively, for the *anti* form and the *syn* conformer. This energy analysis provides insights to compare the nature of interactions of quercetin in the (di)hydrate crystal and in the hIPMK binding site.

4. Conclusions

Ultrahigh-resolution and ultralow-temperature crystal structure determination in the Hansen–Coppens multipole formalism allowed to reveal for the first time the coexistence of both *anti* and *syn* conformers of quercetin compound in the crystalline state. This coexistence is manifested as a very subtle conformational disorder, undetected by standard AIM refinement. Although the structure is disordered, the quality of the synchrotron data and the appropriate constraints imposed during the multipole refinement have led to charge-density characteristics and derived properties that are in good agreement with the literature. The ratio of each conformer reveals that the *anti* conformation is favourable in the dihydrate form while the *syn* conformation is compatible with the presence of only one water molecule. The Hirshfeld surface and contact enrichment ratios analyses together with electrostatic energy values show beyond doubt that hydrogen-bonds involving water molecules are a major driving force in the *anti* crystal packing stabilization. Both the monohydrate and dihydrate crystal packings show a good electrostatic complementarity of quercetin with its surroundings in the regions forming hydrogen bonds. This is not the case in the parallel displaced aromatic stacking involving the two sides of the flat cycles. This finding is supported by the electrostatic energy analysis of both conformers in the crystal clusters constituted of quercetin and water molecules. It appears that in the *anti* dihydrate form, the contribution of the hydrogen bonds to water molecules to the stabilization is stronger than in the *syn* hydrate form. In contrast, the *syn* monohydrate conformer show two strongly attractive quercetin···quercetin dimers, mediated by a double antiparallel O—H/H—O interaction.

With the presence of eight O—H···O and four C—H···O hydrogen bonds (Table 3), the packing shows good electrostatic complementarity between the quercetin molecule and its crystal surroundings. As guest in biological medium where it implements its inhibitor properties against hIMPK kinase, five O—H···O hydrogen bonds are formed between quercetin and the hydrated protein binding site (Table S5). There are, in addition, one N—H···O and six C—H···O hydrogen bonds.

The electrostatic interaction energy of quercetin in the binding site of hIPMK has been quantified and can form a basis for further calculations of the binding affinity between this ligand and the hIPMK protein kinase. The electrostatic interactions energies of protein/ligand contacts are determinant in the orientation of the ligand in the binding site. However, to fully understand the thermodynamics of binding and evaluate the Gibbs free energy change, solvation and entropic effects need also to be analysed by tools such as molecular dynamics (Bradbrook *et al.*, 1998).

Acknowledgements

We acknowledge the European Synchrotron Radiation Facility (ESRF) for provision of synchrotron radiation facilities at beamline ID11 under proposal number HC-1176.

References

Ahmed, M., Jelsch, C., Guillot, B., Lecomte, C. & Domagała, S. (2013). *Cryst. Growth Des.* **13**, 315–325.
Ahmed, M., Yar, M., Nassour, A., Guillot, B., Lecomte, C. & Jelsch, C. (2013). *J. Phys. Chem. A*, **117**, 14267–14275.
Allen, F. H. & Bruno, I. J. (2010). *Acta Cryst.* B**66**, 380–386.
Bader, R. F. W. (1990). *Atoms in Molecules: A Quantum Theory.* Oxford: Clarendon Press.
Bąk, J. M., Dominiak, P. M., Wilson, C. C. & Woźniak, K. (2009). *Acta Cryst.* A**65**, 490–500.
Bibila Mayaya Bisseyou, Y., Bouhmaida, N., Guillot, B., Lecomte, C., Lugan, N., Ghermani, N. & Jelsch, C. (2012). *Acta Cryst.* B**68**, 646–660.
Biovia (2016). Dassault Systèmes, *Discovery Studio Modeling Environment*, release 2017, Dassault Systèmes, San Diego, USA.
Bouhmaida, N., Bonhomme, F., Guillot, B., Jelsch, C. & Ghermani, N. E. (2009). *Acta Cryst.* B**65**, 363–374.
Bradbrook, G. M., Gleichmann, T., Harrop, S. J., Habash, J., Raftery, J., Kalb (Gilboa), J., Yariv, J., Hillier, I. H. & Helliwell, J. R. (1998). *Faraday Trans.* **94**, 1603–1611.
Brock, C. P., Dunitz, J. D. & Hirshfeld, F. L. (1991). *Acta Cryst.* B**47**, 789–797.
Brovarets', O. O. & Hovorun, D. M. (2020*a*). *J. Biomol. Struct. Dyn.* **38**, 2817–2836.
Brovarets', O. O. & Hovorun, D. M. (2020*b*). *J. Biomol. Struct. Dyn.* **38**, 2865–2883.
Bruker (2008). *SADABS*, *SAINT* and *SMART*. Bruker AXS Inc., Madison, Wisconsin, USA.
Bucki, R., Pastore, J. J., Giraud, F., Sulpice, J. C. & Janmey, P. A. (2003). *J. Thromb. Haemost.* **1**, 1820–1828.
Buckingham, A. D. (1959). *Q. Rev. Chem. Soc.* **13**, 183–214.
Cai, W., Chen, Y., Xie, L., Zhang, H. & Hou, C. (2014). *Eur. Food Res. Technol.* **238**, 121–128.
Cushnie, T. P. & Lamb, A. J. (2005). *Int. J. Antimicrob. Agent.* **26**, 343–356.
DeLano, W. (2020). *PyMOL*. https://www.pymol.org.
De Marchi, U., Biasutto, L., Garbisa, S., Toninello, A. & Zoratti, M. (2009). *Biochim. Biophys. Acta*, **1787**, 1425–1432.
Deng, X. H., Song, H. Y., Zhou, Y. F., Yuan, G. Y. & Zheng, F. J. (2013). *Exp. Ther. Med.* **6**, 1155–1158.
Dittrich, B., Fabbiani, F. P. A., Henn, J., Schmidt, M. U., Macchi, P., Meindl, K. & Spackman, M. A. (2018). *Acta Cryst.* B**74**, 416–426.
Dittrich, B., Schürmann, C. & Hübschle, C. B. (2016). *Z. Kristallogr.* **231**, 725–736.
Dittrich, B., Warren, J. E., Fabbiani, F. P. A., Morgenroth, W. & Corry, B. (2009). *Phys. Chem. Chem. Phys.* **11**, 2601–2609.
Dolomanov, O. V., Bourhis, L. J., Gildea, R. J., Howard, J. A. K. & Puschmann, H. (2009). *J. Appl. Cryst.* **42**, 339–341.
Domagała, S., Fournier, B., Liebschner, D., Guillot, B. & Jelsch, C. (2012). *Acta Cryst.* A**68**, 337–351.
Domagała, S., Munshi, P., Ahmed, M., Guillot, B. & Jelsch, C. (2011). *Acta Cryst.* B**67**, 63–78.
Dorta, D. J., Pigoso, A. A., Mingatto, F. E., Rodrigues, T., Pestana, C. R., Uyemura, S. A., Santos, A. C. & Curti, C. (2008). *Phytother. Res.* **22**, 1213–1218.
Dorta, D. J., Pigoso, A. A., Mingatto, F. E., Rodrigues, T., Prado, L. M. R., Helena, A. F. C., Uyemura, S. A., Santos, A. C. & Curti, C. (2005). *Chem. Biol. Interact.* **152**, 67–78.
Duarte, J., Pérez–Palencia, R., Vargas, F., Angeles Ocete, M., Pérez–Vizcaino, F., Zarzuelo, A. & Tamargo, J. (2001). *Br. J. Pharmacol.* **133**, 117–124.
Dubey, R. & Desiraju, G. R. (2015). *IUCrJ*, **2**, 402–408.
Edwards, R. L., Lyon, T., Litwin, S. E., Rabovsky, A., Symons, J. D. & Jalili, T. (2007). *J. Nutr.* **137**, 2405–2411.
Espinosa, E. & Molins, E. (2000). *J. Chem. Phys.* **113**, 5686–5694.
Espinosa, E., Molins, E. & Lecomte, C. (1998). *Chem. Phys. Lett.* **285**, 170–173.
Farrugia, L. J. (2012). *J. Appl. Cryst.* **45**, 849–854.
Filip, X., Grosu, I. G., Miclăuş, M. & Filip, C. (2013). *CrystEngComm*, **15**, 4131–4142.
Gatti, C. (2005). *Z. Kristallogr. Cryst. Mater.* **220**, 399–457.
Gatto, M. T., Falcocchio, S., Grippa, E., Mazzanti, G., Battinelli, L., Nicolosi, G., Lambusta, D. & Saso, L. (2002). *Bioorg. Med. Chem.* **10**, 269–272.
Grädler, U., Gerber, H. D., Goodenough-Lashua, D. M., Garcia, G. A., Ficner, R., Reuter, K., Stubbs, M. T. & Klebe, G. (2001). *J. Mol. Biol.* **306**, 455–467.
Gu, C., Stashko, M. A., Puhl-Rubio, A. C., Chakraborty, M., Chakraborty, A., Frye, S. V., Pearce, K. H., Wang, X., Shears, S. B. & Wang, H. (2019). *J. Med. Chem.* **62**, 1443–1454.
Guillot, B., Enrique, E., Huder, L. & Jelsch, C. (2014). *Acta Cryst.* A**70**, C279.
Hansen, N. K. & Coppens, P. (1978). *Acta Cryst.* A**34**, 909–921.
Holstein, J. J., Luger, P., Kalinowski, R., Mebs, S., Paulman, C. & Dittrich, B. (2010). *Acta Cryst.* B**66**, 568–577.
Huggins, D. J. & Tidor, B. (2011). *Protein Eng. Des. Sel.* **24**, 777–789.
Islam, M. R., Zaman, A., Jahan, I., Chakravorty, R. & Chakraborty, S. (2013). *J. Young Pharm.* **5**, 173–179.
Jelsch, C., Devi, R. N., Noll, B. C., Guillot, B., Samuel, I. & Aubert, E. (2020). *J. Mol. Struct.* **1205**, 127600.
Jelsch, C., Ejsmont, K. & Huder, L. (2014). *IUCrJ*, **1**, 119–128.
Jelsch, C., Guillot, B., Lagoutte, A. & Lecomte, C. (2005). *J. Appl. Cryst.* **38**, 38–54.
Jelsch, C., Miteva, M. & Guillot, B. (2023). European Patent EP4195210.
Jin, G.-Z., Yamagata, Y. & Tomita, K. (1990). *Acta Cryst.* C**46**, 310–313.
Klitou, P., Rosbottom, I. & Simone, E. (2019). *Cryst. Growth Des.* **19**, 4774–4783.
Kumar, R., Vijayalakshmi, S. & Nadanasabapathi, S. (2017). *Def. Life. Sc. Jl.* **2**, 142–151.
Lamson, D. W. & Brignall, M. S. (2000). *Altern. Med. Rev.* **5**, 196–208.
Leopoldini, M., Marino, T., Russo, N. & Toscano, M. (2004). *Theor. Chem. Acc.* **111**, 210–216.
Li, Z., Moalin, M., Zhang, M., Vervoort, L., Hursel, E., Mommers, A. & Haenen, G. R. M. M. (2020). *Int. J. Mol. Sci.* **21**, 6015.
Madsen, A. Ø. & Hoser, A. A. (2014). *J. Appl. Cryst.* **47**, 2100–2104.
Magalingam, K. B., Radhakrishnan, A. & Haleagrahara, N. (2014). *BMC Res. Notes*, **7**, 49.
Martinez, C. R. & Iverson, B. L. (2012). *Chem. Sci.* **3**, 2191–2201.
McKinnon, J. J., Mitchell, A. S. & Spackman, M. A. (1998). *Chem. Eur. J.* **4**, 2136–2141.
McKinnon, J. J., Spackman, M. A. & Mitchell, A. S. (2004). *Acta Cryst.* B**60**, 627–668.
Meindl, K. & Henn, J. (2008). *Acta Cryst.* A**64**, 404–418.
Meindl, K., Henn, J., Kocher, N., Leusser, D., Zachariasse, K. A., Sheldrick, G. M., Koritsanszky, T. & Stalke, D. (2009). *J. Phys. Chem. A*, **113**, 9684–9691.
Minini, M., Senni, A., Unfer, V. & Bizzarri, M. (2020). *Molecules*, **25**, 4401.
Mladenovic, M., Arnone, M., Fink, R. F. & Engels, B. (2009). *J. Phys. Chem. B*, **113**, 5072–5082.
Nguyen, D., Macchi, P. & Volkov, A. (2020). *Acta Cryst.* A**76**, 630–651.
Nguyen, D. & Volkov, A. (2019). *Acta Cryst.* A**75**, 448–464.
Olejniczak, S. & Potrzebowski, M. J. (2004). *Org. Biomol. Chem.* **2**, 2315–2322.
Oršolić, N., Knežević, A. H., ŠVer, L., Terzić, S. & Bašić, I. (2004). *J. Ethnopharmacol.* **94**, 307–315.
Pal, R., Jelsch, C., Momma, K. & Grabowsky, S. (2022). *Acta Cryst.* B**78**, 231–246.
Rajalakshmi, G., Hathwar, V. R. & Kumaradhas, P. (2014). *Acta Cryst.* B**70**, 568–579.
Rossi, M., Rickles, L. F. & Halpin, W. A. (1986). *Bioorg. Chem.* **14**, 55–69.

Ruiz, L. M., Salazar, C., Jensen, E., Ruiz, H. P., Tiznado, W., Quintanilla, R. A., Barreto, M. & Elorza, A. A. (2015). *Oxid. Med. Cell. Longev.* **2015**, 836301.
Russo, N., Toscano, M. & Uccella, N. (2000). *J. Agric. Food Chem.* **48**, 3232–3237.
Shi, G. J., Li, Y., Cao, Q. H., Wu, H. X., Tang, X. Y., Gao, X. H., Yu, J. Q., Chen, Z. & Yang, Y. (2019). *Biomed. Pharmacother.* **109**, 1085–1099.
Spackman, M. A. & Byrom, P. G. G. (1997). *Chem. Phys. Lett.* **267**, 215–220.
Spackman, M. A., McKinnon, J. J. & Jayatilaka, D. (2008). *CrystEngComm*, **10**, 377–388.
Spackman, P. R., Turner, M. J., McKinnon, J. J., Wolff, S. K., Grimwood, D. J., Jayatilaka, D. & Spackman, M. A. (2021). *J. Appl. Cryst.* **54**, 1006–1011.
Thong, N. M., Vo, Q. V., Huyen, T. L., Bay, M. V., Tuan, D. & Nam, P. C. (2019). *ACS Omega*, **4**, 14996–15003.
Torres, S., Ferraudi, G., Aguirre, M. J., Isaacs, M., Matsuhiro, B., Chandía, N. P. & Mendoza, L. (2011). *Helv. Chim. Acta*, **94**, 293–300.
Vasilescu, D. & Girma, R. (2002). *Int. J. Quantum Chem.* **90**, 888–902.
Volkov, A., Koritsanszky, T. & Coppens, P. (2004*a*). *Chem. Phys. Lett.* **391**, 170–175.
Volkov, A., Li, X., Koritsanszky, T. & Coppens, P. (2004*b*). *J. Phys. Chem. A*, **108**, 4283–4300.
Vuković, V., Leduc, T., Jelić-Matošević, Z., Didierjean, C., Favier, F., Guillot, B. & Jelsch, C. (2021). *Acta Cryst.* D**77**, 1292–1304.
Wawer, I. & Zielinska, A. (1997). *Solid State Nucl. Magn. Reson.* **10**, 33–38.
Williams, C. J., Headd, J. J., Moriarty, N. W., Prisant, M. G., Videau, L. L., Deis, L. N., Verma, V., Keedy, D. A., Hintze, B. J., Chen, V. B., Jain, S., Lewis, S. M., Arendall, W. B. III, Snoeyink, J., Adams, P. D., Lovell, S. C., Richardson, J. S. & Richardson, D. C. (2018). *Protein Sci.* **27**, 293–315.
Wilson, A. J. C. (1942). *Nature*, **150**, 152.
Wu, G., Rodrigues, B. L. & Coppens, P. (2002). *J. Appl. Cryst.* **35**, 356–359.
Zamin, L. L., Filippi-Chiela, E. C., Dillenburg-Pilla, P., Horn, F., Salbego, C. & Lenz, G. (2009). *Cancer Sci.* **100**, 1655–1662.
Zheng, Y. Z., Deng, G., Liang, Q., Chen, D. F., Guo, R. & Lai, R. C. (2017). *Sci. Rep.* **7**, 7543.